

COVER SHEET

*NOTE: This coversheet is intended for you to list your article title and author(s) name only
—this page will not appear on the CD-ROM.*

Paper Number: **1500** (*replace with your paper number*)

Title: **An enriched shell element for delamination simulation in composite laminates**

Authors: Mark McElroy

ABSTRACT

A formulation is presented for an enriched shell finite element capable of delamination simulation in composite laminates. The element uses an adaptive splitting approach for damage characterization that allows for straightforward low-fidelity model creation and a numerically efficient solution. The Floating Node Method is used in conjunction with the Virtual Crack Closure Technique to predict delamination growth and represent it discretely at an arbitrary ply interface. The enriched element is verified for Mode I delamination simulation using numerical benchmark data. After determining important mesh configuration guidelines for the vicinity of the delamination front in the model, a good correlation was found between the enriched shell element model results and the benchmark data set.

INTRODUCTION

Progressive damage simulation in composite laminates using finite elements is often performed using models consisting of solid elements with a mesh refinement of at least one element per ply. This level of high-fidelity is necessary with current simulation techniques to be able to predict and represent physically complex three-dimensional damage processes through the thickness of a laminate. Excessive computational demand and required user expertise for complex high-fidelity simulations, however, often limit the use of these tools in practice by driving up the time and cost associated with a given analysis. As the continuous advancement of computational technology allows for increasingly complex models and shorter run times, the cost of necessary user training and the required time for model creation and verification still may remain high.

Model fidelity is typically high for two reasons. The first reason is the need for detailed stress and strain information to be available through each ply for a criterion to use for prediction of initiation and propagation of a laminate damage process such as matrix cracking or delamination. The second reason for high model fidelity is simply to have a mesh capable of representation of a three-dimensional damage pattern as dictated by the damage growth criterion. The price paid for high-fidelity models such as this, in general, is that they are very inefficient as a large amount of information is determined throughout the entire model when this level of detail is only needed at locations where a damage process is occurring.

Shell elements have long been used by industry for analyses that are less complex than laminate damage simulation and have proven to be a cost effective analysis tool. Shell element models are computationally efficient, and due to a simplified mesh when compared to a high-fidelity solid element approach, the models are inherently less expensive for an analyst to create and use. Use of shell element models for laminate damage simulation, however, introduces a number of challenges, the most obvious of which may be prediction and characterization of out of plane transverse matrix cracks and delaminations at multiple interfaces. A fundamental prerequisite for modeling a complex damage process such as this is the use of shells to simulate simple delamination problems that do not include matrix crack interaction. This capability should be demonstrated before further work towards use of shells for a more complex three-dimensional simulation is undertaken.

Layer-wise stacking is a common technique for using shell elements for laminate damage simulation [1,2]. In such an approach, independent layers of shell elements are defined and connected across ply interfaces in a laminate. If delamination at a specific ply interface is of interest, a mesh may consist of two layers of shell elements, one on either side of the ply interface location. The two layers can be connected by rigid links and delamination growth can be simulated using the Virtual Crack Closure Technique (VCCT) [3,4]. Wang et al. [5] were among the first to study the use of VCCT for delamination growth in this manner and presented formulas for calculation of energy release rates using shell elements. This work, along with a related study later [6], indicate that mixed-mode energy release rate can be calculated using shell elements, however, continued mesh refinement may not result in converged values in some cases. Similarly, in bimaterial crack tip interfaces, energy release rate component divergence is observed during mesh refinement when using VCCT with any element type. Previous work indicated that this non-convergence may be avoided by sizing the mesh above a

minimum value based on the ratio of crack growth length (i.e., mesh size) to element thickness, $\Delta a/h$ [7].

An inherent disadvantage of the two-layer stacked shell models is that the delamination interface must be predefined, thereby limiting the model's utility as a general predictive tool. Furthermore, by restricting the delamination to a single ply interface location, multiple delaminations, or delamination and matrix crack interaction, is not possible. One means to avoid this is to model many or all interfaces in the mesh where there is an independent layer of shells for every ply. This type of approach, however, begins to share some of the same drawbacks mentioned for high-fidelity solid element models. Ideally, in terms of computational efficiency and ease of use, a laminate would be modeled as a single layer of shell elements where a delamination could form and propagate at an arbitrary location in the layup. This approach has been enabled for through thickness cracks by numerical simulation techniques such as the Extended Finite Element Method (XFEM) [8], the Phantom Node Method (PNM) [9], and the Floating Node Method (FNM) [10]. The same concept can be applied to delamination in shell elements, but the arbitrary discontinuity is constrained to be orthogonal to the shell surface normal. The fidelity required for damage growth in a model such as this can be thought of as adaptive in that the model is defined initially in low-fidelity, one element thick, and remains in this state everywhere except locally where delamination occurs and multiple layers are required. Simulation models based on shell elements that allow for an arbitrary delamination location and adaptive fidelity through the thickness have been proposed and studied only recently [11-13].

The goal of this paper is to present the formulation and initial verification of a novel enriched shell element capable of delamination simulation in composite laminates. The element enrichment allows for adaptive mesh fidelity through the thickness where a single element splits into two elements only as required locally to characterize an evolving delamination process. At any location in the model where damage does not occur, the original discretization remains unaffected and a single shell element is used to represent the entire laminate thickness as defined in the beginning of the analysis. This capability is achieved using the Floating Node Method [10] to discretely represent a delamination in the mesh and VCCT to predict its growth. The element is coded as a user-subroutine in Abaqus 6.14/Standard® [14]. Details concerning the use of VCCT in conjunction with shell elements, mesh dependency of the solution (i.e., $\Delta a/h$ ratio), and delamination fronts misaligned with the mesh are investigated. This study serves as the first milestone of the enriched shell element's development process where the ultimate goal is to include the capability to simulate mixed-mode delaminations and transverse matrix crack-delamination interactions.

ELEMENT FORMULATION

Mindlin Shell Element

The enriched finite element is based on a linear four node, six degrees of freedom (DOF) per node, Mindlin shell as presented by Onate [15]. The element has the ability to undergo transverse shear deformation and performs well for both thick and thin shells. Transverse shear correction factors are determined layer-wise as proposed by [16].

Shear locking is eliminated by imposing an assumed linear distribution of transverse shear strain in the element as described by Onate [15]. Full four point Gaussian integration is used to calculate the stiffness matrix. Classical laminate theory is used to determine orthotropic bulk material properties for the element based on a layup of differing ply orientations.

Implementation of the Floating Node Method (FNM)

The FNM works by embedding extra unused nodes as “floating DOF” into an element stiffness matrix as rows and columns of zeroes. If and when an element is split (see VCCT criteria in the next section), the floating DOF are activated and used to define what is effectively an additional element but still within the original element definition. Numerically, the FNM functions as follows. The stiffness matrix, $K^{(e)}$, without any type of discontinuity in the displacement field, is determined by integration across the element area in the x - and y -directions and the element thickness, h , in the z -direction and is given by

$$K^{(e)} = \int_x \int_y H^T \left[\int_z C dz \right] H dy dx = \int_b \int_b H^T \left[\int_{-\frac{h}{2}}^{\frac{h}{2}} C dz \right] H dy dx \quad (1)$$

where H , a function of four linear shape functions, is the strain-displacement matrix, C is the constitutive material matrix, and b is the edge dimension of a square element. In a laminate shell formulation, C may be defined as a function of submatrices A , B , D , and G known from classical laminate theory that correspond to membrane, membrane-bending coupling, bending, and transverse shear behavior respectively. The A , B , D , and G matrices for a laminate are determined by

$$A = \int_{-\frac{h}{2}}^{\frac{h}{2}} C_p dz, \quad B = \int_{-\frac{h}{2}}^{\frac{h}{2}} z C_p dz \quad (2a \ \& \ 2b)$$

$$D = \int_{-\frac{h}{2}}^{\frac{h}{2}} z^2 C_p dz, \quad G = \int_{-\frac{h}{2}}^{\frac{h}{2}} C_s dz \quad (2c \ \& \ 2d)$$

where C_p and C_s correspond to planar and transverse shear constitutive material properties, respectively. Equation (1) for a laminate shell can be re-written as

$$K^{(e)} = \int_b \int_b H^T \left[\int_{-\frac{h}{2}}^{\frac{h}{2}} C(A, B, D, G) dz \right] H dy dx \quad (3)$$

When a discontinuity is introduced at a single uniform z -coordinate, as in the case of a delamination, the element material is split into two regions, Ω_A and Ω_B , where region Ω_B corresponds to the DOF of the floating nodes. The stiffness matrix for a split element is given by

$$K^{(e)} = K_{\Omega_A}^{(e)} + K_{\Omega_B}^{(e)} \quad (4)$$

where $K_{\Omega_A}^{(e)}$ and $K_{\Omega_B}^{(e)}$ are determined using equation (3), but with their respective material integration limits split along the z -axis according to the discontinuity location. A diagram of an element in a damaged and undamaged state with associated stiffness matrices is shown in Figure 1. While the FNM has been used before in combination with VCCT [17], it has yet to be implemented in shell elements for in-plane delamination damage modeling as described.

Currently, the FNM is implemented in the enriched element such that one delamination is possible, however, multiple delaminations could be handled with the same approach. As such, the element is defined with eight nodes total, four “real nodes” used in the definition of the initial undamaged region and four “floating nodes” used in the event that the element is split. There are 6 DOF per node resulting in a total of 48 DOF per element. Computational efficiency is achieved by only performing stiffness integration across “activated” regions thereby numerically treating undamaged elements as if they were non-enriched conventional shell elements. This concept is illustrated by the stiffness matrix formulas shown in Figure 1. Unused floating nodes, as rows and columns of zeros, are removed from the global stiffness matrix by the Abaqus[®] solver reducing total DOF and effectively rendering undamaged elements back to a non-enriched state for the solution of equilibrium equations at each load increment.

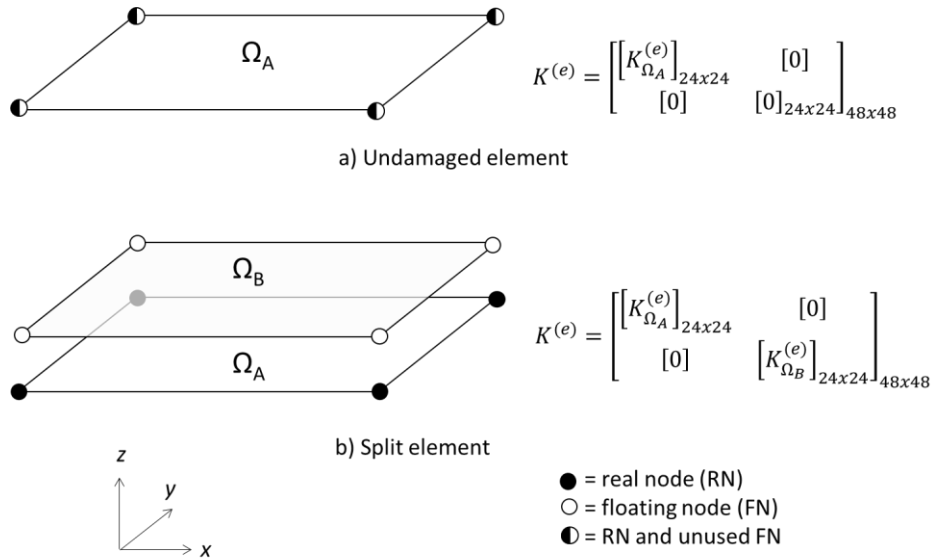
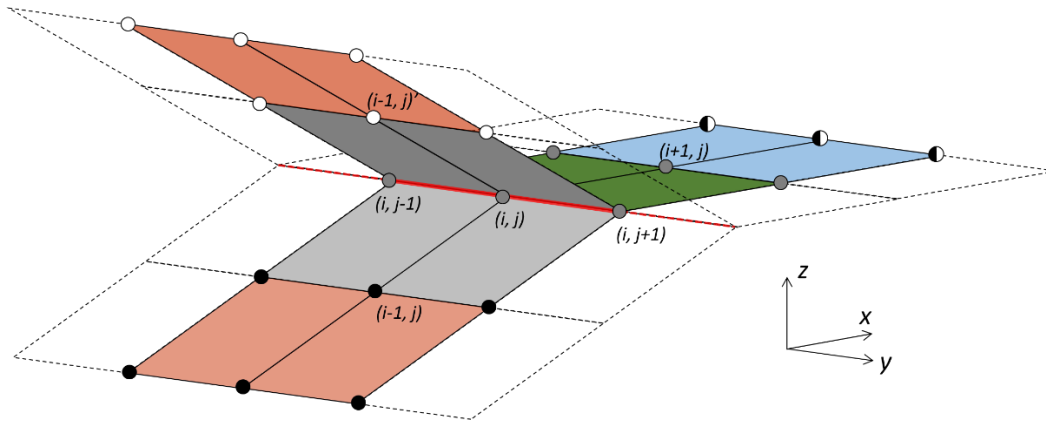


Figure 1. Shell element damage states.

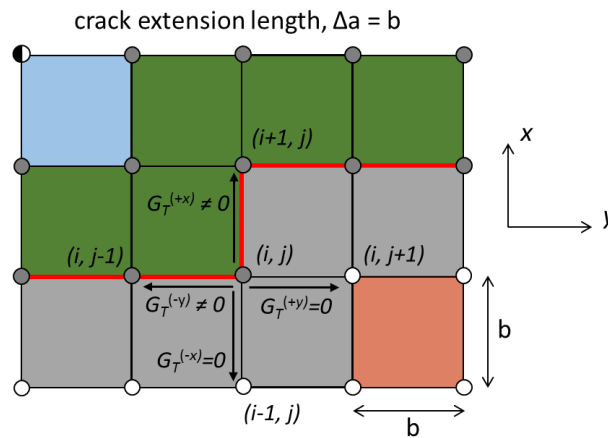
VCCT and Damage Progression

The enriched shell element can be used in a mesh to represent four different damage states. These are illustrated in Figure 2a and consist of 1) undamaged element, 2) split element ahead of the crack tip with all nodes tied, 3) split element at the crack tip with one or more nodes free, and 4) split element in the crack wake with all nodes free. At

the end of every solution increment, VCCT is used on each delamination front tied node to determine if the tie should remain in place or be released resulting in a change in the adjacent element damage states (same as [18]). The tied nodes are constrained by inserting stiff springs internal to an element stiffness matrix connecting real and floating DOF (spring stiffness = 10^6 N/mm).



a) Straight delamination front aligned with mesh



b) Plan view of staggered delamination front with possible growth paths that the simulation considers at a corner crack tip node i, j .

- = undamaged element
- = split element ahead of crack tip w/all nodes tied
- = split element at crack tip w/one or more nodes tied
- = split element in wake of crack tip w/all nodes free
- = delamination front
- = real node (RN)
- = floating node (FN)
- = RN tied to FN
- = RN & unused FN
- (i, j) = node designation

All nodes have 6 global DOF $u, v, w, \theta_x, \theta_y, \theta_z$ associated with nodal forces $F_x, F_y, F_z, M_x, M_y, M_z$ respectively

Figure 2. Delamination front mesh description.

In general, the use of VCCT is relatively straightforward when the mesh is aligned with the delamination front. However, when the delamination front and mesh are misaligned, the application of VCCT may not be intuitive. Methods have been proposed to implement VCCT such that it can be used accurately to simulate delamination growth independent of mesh alignment. One such approach involves determination of a growth direction vector which is used to calculate the required crack growth area and the location where the crack opening displacements are obtained [19,20]. Alternatively, Orifici et al. [18] presented an approach where correction factors are applied at delamination front nodes depending on the connectivity of the neighboring nodes. The approach used in the current study is less elaborate than any of these methods.

Figure 2b can be seen as an example of a small section of a staggered delamination front where globally neither the shape of the front nor the direction of propagation is aligned with the mesh. VCCT is applied at the corner node (i,j) to calculate the total energy release rate, G_T . The application of VCCT in the enriched shell element is based on an assumption that at a given tied crack front node, the delamination can only advance in orthogonal directions along mesh lines and therefore always obtains wake displacements at nodal locations. At the end of an increment, the energy release rate at a tied node is calculated in four directions parallel to the mesh: $+x$, $-x$, $+y$, and $-y$ as shown in Figure 2b. Using delamination growth in the positive x -direction as an example, Mode I, Mode II, and total energy release rates at node (i,j) are determined using formulas from [5] given as

$$G_I^{(+x)} = \frac{-1}{2\Delta A^{(e)}} \left[F_z^{(i,j)} (w^{(i-1,j)'} - w^{(i-1,j)}) + M_x^{(i,j)} (\theta_x^{(i-1,j)'} - \theta_x^{(i-1,j)}) + M_y^{(i,j)} (\theta_y^{(i-1,j)'} - \theta_y^{(i-1,j)}) \right] \quad (5)$$

$$G_{II}^{(+x)} = \frac{-1}{2\Delta A^{(e)}} \left[F_x^{(i,j)} (u^{(i-1,j)'} - u^{(i-1,j)}) \right] \quad (6)$$

$$G_T^{(+x)} = G_I^{(+x)} + G_{II}^{(+x)} \quad (7)$$

where F , M , w , u , and θ are nodal force, moment, z -displacement, x -displacement, and rotation, respectively. Nodal designations with a prime superscript refer to the “upper” set of elements (i.e., floating nodes) and crack extension area, $\Delta A^{(e)} = b^2$, is the area of an element for a square regular mesh (in the current form of the VCCT implementation in the element enrichment, the mesh is required to consist of regular square elements). The critical energy release rate, G_c , is obtained using the Benzeggagh-Kenane criterion [21]

$$G_c^{(+x)} = G_{Ic} + (G_{IIc} - G_{Ic}) \left(G_{II}^{(+x)} / G_T^{(+x)} \right)^{\eta_{BK}} \quad (8)$$

where G_{Ic} and G_{IIc} are fracture toughness properties of the material and η_{BK} is a curve fit parameter determined from testing.

G_T and G_c are calculated in the other three propagation directions, $-x$, $+y$, and $-y$, by changing the wake displacement location, $(i-1,j)$, in equations (5) and (6) to $(i+1,j)$, $(i,j-1)$, and $(i,j+1)$, respectively. The maximum G_T , out of the four possible propagation directions, is then compared to G_c and if $G_T > G_c$, the tie is released. Even though the

enriched shell considers four possible growth directions, those that do not have any physical meaning (i.e., such as “reverse” growth in the $-x$ -direction in Figure 2a, etc.), produce $G_T = 0$. If a delamination front node has more than one non-zero G_T , such as the corner node (i,j) in Figure 2b, only the maximum G_T has any bearing on whether or not that tie is released.

Mesh Configuration Near the Delamination Front

It was found that when modeling a double cantilever beam (DCB) specimen the constrained DOF in the ties at the delamination front and the number of split (but still tied) elements ahead of the delamination front both affect the element performance significantly. Therefore, three cases were considered as summarized in Table I. In Case 3, the number of split elements is based on a distance ahead of the delamination front and therefore varies between mesh sizes. The number of split elements ahead of the delamination front is maintained as the front advances in the simulations.

TABLE I. SUMMARY OF THREE CASES CONSIDERED VARYING DELAMINATION FRONT TIED DOF AND NUMBER OF ELEMENTS SPLIT BUT TIED AHEAD OF THE DELAMINATION.

Case	DOF tied	Number of elements split ahead of crack tip
1	$u, v, w, \theta_x, \theta_y, \theta_z$	1
2	u, v, w	1 7, mesh = 1.0 mm
3	u, v, w	4, mesh = 2.5 mm 2, mesh = 5.0 mm

Due to the symmetric nature of the DCB specimen configuration and loading, each bending arm can be thought of as a cantilever beam supported at the crack tip with a point load at the end. The boundary condition at the crack tip is somewhat complex as the material supporting the bending arms ahead of the crack tip can deform in the axial direction and effectively allow a small amount of rotation. This root rotation would be captured in a high-fidelity model where the specimen is meshed through the thickness with multiple elements, however, this level of mesh fidelity is not present in a beam or shell model. Cotterell et al. proposed a method to simulate a small amount of root rotation in a simple beam model by increasing total crack length (i.e. increasing flexibility) [22], but it is not immediately obvious if this type of approach is viable in a general three-dimensional model. The three Cases described in Table I are investigated in an attempt to determine an accurate means to include the effects of root rotation in the structural stiffness of the specimen.

Case 1 has rotations constrained in the ties at the delamination front and therefore does not account for any root rotation. Case 2 is considered as means to ‘relax’ the boundary condition present in Case 1 and allow some form of root rotation. Case 1 and Case 2 are compared in Figure 3 using two beam models representative of the upper DCB bending arm in each case. By summing forces and moments and comparing analytical beam deflection formulae, it is shown that in Case 2, the tie forces located at the crack tip and beam deflections to be used in VCCT calculations are a function of mesh size, b .

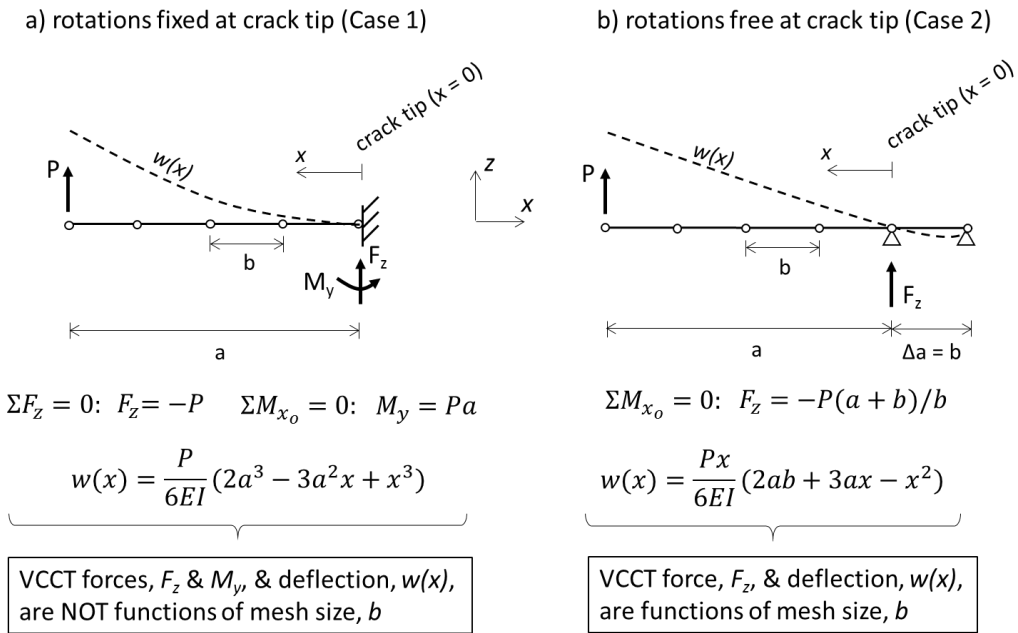
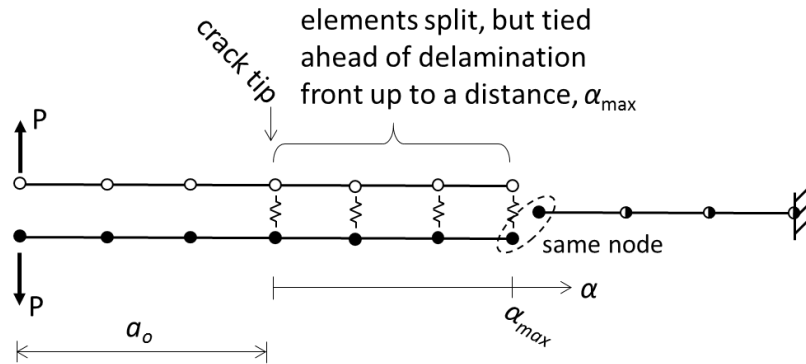


Figure 3. VCCT force and deflection dependency on constrained DOF at crack tip for Case 1 and Case 2.

Case 3 is considered as a means to correct the mesh dependency in Case 2 while still providing a ‘relaxed’ boundary condition when compared to Case 1 that effectively allows some root rotation. A diagram of the Case 3 mesh is shown in Figure 4 where multiple elements are split ahead of the delamination front along the axis α up to a distance of α_{max} .



Note: split elements are shown as offset for illustrative purposes only

- = real node (RN)
- = floating node (FN)
- ◐ = RN & unused FN

Figure 4. Diagram of mesh for Case 3: rotations are unconstrained in split element ties and multiple elements ahead of the delamination are split and tied together.

ANALYSIS

Results from a numerical Double Cantilever Beam (DCB) benchmark study [23] were used to verify the enriched shell element's capability to simulate Mode I delamination. All analyses were static with linear ramping loads and run in Abaqus 6.14/Standard® [14]. The enriched shell element was coded in a user defined element subroutine (UEL). Models were created using the enriched shell element with three mesh sizes for Cases 1 – 3. The mesh sizes considered, 1.0 mm, 2.5 mm, and 5.0 mm, correspond to $\Delta a/h$ ratios of 0.66, 1.33, and 3.33, respectively, where Δa is crack extension length and h is the thickness of one region of a split element. A schematic of the DCB test specimen and an overview of the finite element model are shown in Figure 5. Because the model consists of planar coincident shell elements, it is shown in a deformed state to better illustrate its features. Material properties for the specimen are given in Table II [23]. Only Mode I verification is presented in this paper, though work is ongoing regarding Mode II and mixed-mode delaminations.

TABLE II. MATERIAL PROPERTIES FOR DCB SPECIMEN: T300/1076 [23].

Parameter	Value	Units
E_{11}	139.4	GPa
E_{22}	10.16	GPa
E_{33}	10.16	GPa
G_{12}	4.6	GPa
G_{13}	4.6	GPa
G_{23}	3.54	GPa
ν_{12}	0.3	-
ν_{13}	0.3	-
ν_{23}	0.436	-
G_{Ic}	0.17	kJ/m ²
G_{IIc}	0.494	kJ/m ²
η_{BK}	1.62	-

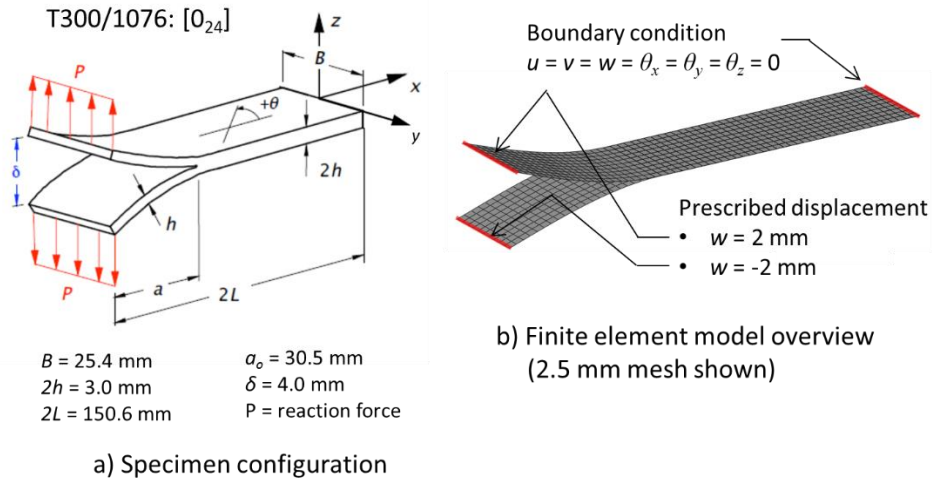


Figure 5. DCB specimen.

RESULTS & DISCUSSION

Force displacement correlations are shown in Figure 6 for Cases 1-3. In all cases, the “sawtooth” behavior seen in the force displacement curves can be explained by the sudden release of a tied crack tip node as the delamination advances one element length. This behavior is seen to diminish with mesh refinement. In Case 1, based on the close match for the critical force magnitude seen in Figure 6a, the energy release rate appears to be predicted well but the stiffness of the model prior to damage is over predicted by approximately 24%. Also of note in the Case 1 results is that no mesh dependency is seen concerning stiffness or energy release rate prediction. Both of these observations are in accordance with the beam analysis previously shown in Figure 3a.

Case 2 does not constrain rotations in the ties and splits one element ahead of the delamination. It is clear from Figure 6b that while it is possible to match the stiffness well with this approach, both the stiffness and energy release rate are mesh dependent. These observations also are in accordance with the beam analysis shown previously in Figure 3b.

Results from the Case 3 configuration, where tie rotations are unconstrained and more than one element ahead of the delamination is split, are shown in Figure 6c. Case 3 was found to produce accurate stiffness and energy release rate results and remove the mesh dependency seen in Case 2. The applied force at a given displacement for Case 3 generally is under predicted by approximately 5% for all mesh sizes, although at the critical value where damage initiates, the error is <1%.

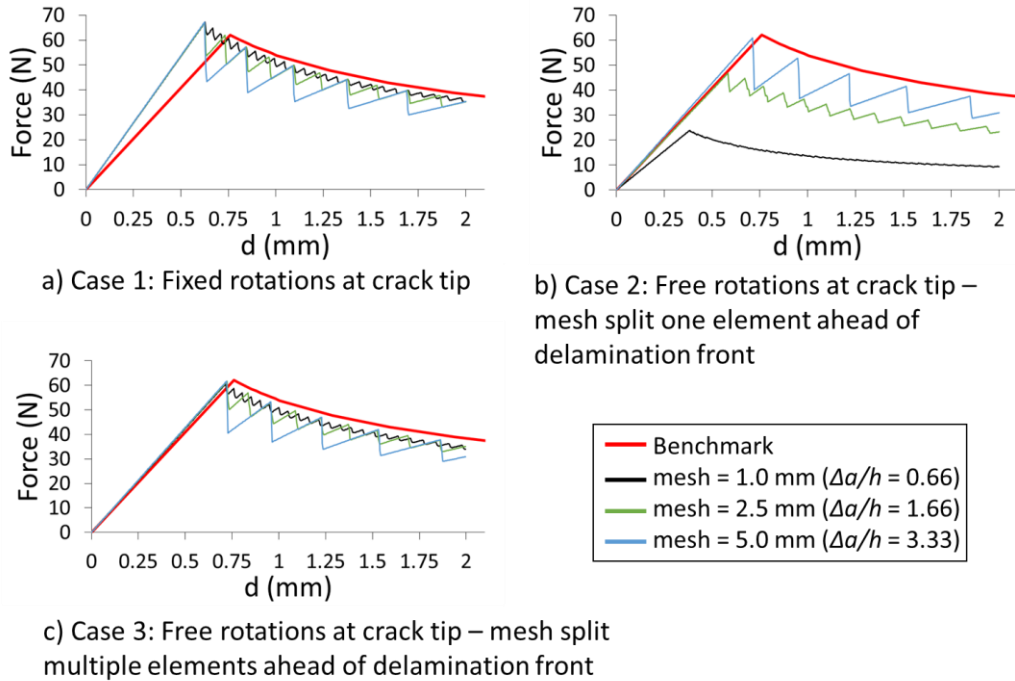


Figure 6. DCB: Force displacement data correlation.

A closer examination of the Case 3 model behavior is helpful to understand its functionality in more detail. A version of the Case 3 model for each mesh size was created where all elements up to 15.0 mm away from the delamination front were split and tied together (i.e., $\alpha_{\max} = 15.0$ mm). To suit this condition, 15, 6, and 3 elements are split ahead of the delamination front in the 1.0 mm, 2.5 mm, and 5.0 mm mesh models, respectively. Using these modified Case 3 models, the force, F_z , in each of the nodal ties in the split elements is normalized by the value at the crack tip and plotted in Figure 7b versus α . The definitions for α and α_{\max} are shown again in Figure 7a for convenience. Figure 7b shows that the applied DCB load is not carried entirely by one or two ties in the vicinity of the crack tip, as Case 2 effectively assumes, but by as many nodes as are present in a fixed distance ahead of the delamination front.

The tie force in all mesh sizes is seen in Figure 7b to converge to zero at approximately $\alpha = 10.0$ mm indicating that in this particular DCB specimen, all nodes within the range of $0 \leq \alpha \leq 10.0$ mm help to resist the applied load. Intuitively then, if there are not ties present within the 10.0 mm range or up until the force has sufficiently vanished, the applied load is resisted globally by what amounts to an inaccurate boundary condition for the DCB bending arms. This is what happens in Case 2 where there is only one node resisting the applied load ahead of the delamination. Figure 7b also illustrates why the 5.0 mm mesh is the most accurate within Case 2 as the single supporting node ahead of the delamination is located further along the curve closer to the point where the tie loads vanish. At the time of this paper, a generally applicable method to determine the distance required to split elements ahead of the delamination has not been determined.

Figure 7c compliments the previous conclusions made using Figure 7b. Energy release rate convergence for each Case 3 mesh is plotted versus α_{max} . Note that the first data point for each curve in this plot is equivalent to Case 2. In all curves, energy release rate is obtained from a node halfway across the specimen width at a common, but arbitrary, load step prior to any damage initiation. Energy release rate predicted by all meshes converges to the same value which also matches an analytical solution [24] given by

$$G_I = \frac{P^2 a^2}{BEI} \quad (9)$$

where P is the applied load, a is the initial crack length, B is the specimen width, E is the stiffness modulus set equal to E_{II} here, and I is the area moment of inertia.

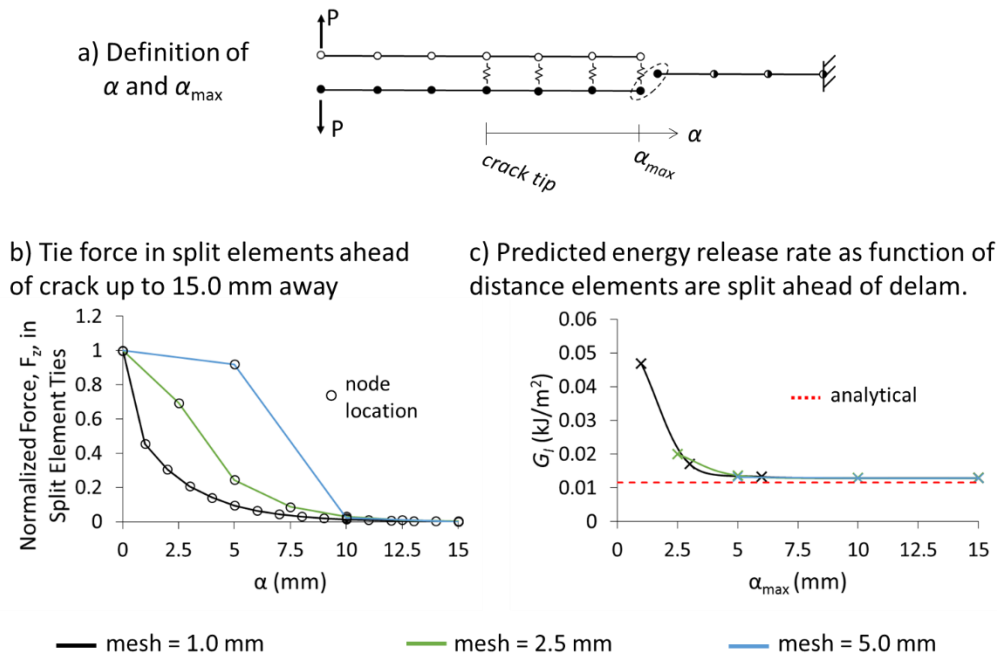


Figure 7. Tie forces in split elements ahead of the crack tip and G_I as a function of distance elements are split ahead of delamination.

The remaining results are shown for Case 3 (as described in Table I) only. Figure 8 is a plot of energy release rate normalized by G_c across the delamination front. The data shown correspond to the load increment just before the first instance of damage growth. Results from each mesh size are included along with an analytical solution given by equation (9). While some small variance can be seen, there does not appear to be an appreciable amount of mesh dependence on energy release rate calculation for the mesh sizes considered. An exception to this is at the edges where the resolution in the finer meshes allows the drop in G to be characterized in more detail. The average G_I from the 1.0 mm mesh model has an error of approximately 5% when compared to the analytical solution. This amount of error agrees with a similar observation made in the force

displacement curves in Figure 6c. Based on Figure 6c and Figure 8, meshes using the Case 3 conditions sized corresponding to a $\Delta a/h$ ratio range of 0.66 – 3.33, where Δa is the mesh size and h is half of the total laminate thickness, will produce accurate energy release rates in the enriched element for Mode I delaminations.

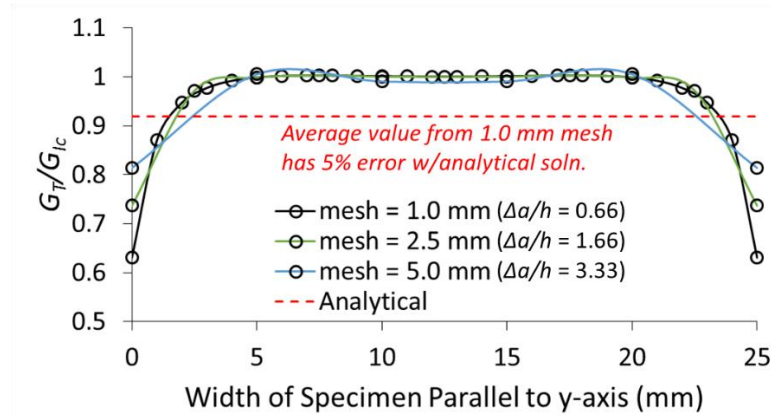


Figure 8. DCB: Results from mesh convergence study for normalized energy release rate, G_T/G_{Ic} , distribution across delamination front ($a = a_o = 30.5$ mm).

In Figure 9a, the DCB model with a 1.0 mm mesh is shown in plan view at the end of a load increment identified as “Frame 1” just prior to the load step where G_T exceeds G_C for the first time. For illustrative purposes, a two-tone contour plot of deflection in the z -direction (i.e. out-of-plane) is shown where the lighter gray represents deflections greater than $z = 0$ ($z = 0$ lies on the specimen mid-plane). In this manner, elements that are delaminated can be identified by the fact that they have split and are deflected upwards in the positive z -direction. Following Frame 1, sequential load increments, Frames 2-5 seen in Figures 9b-9e, demonstrate the process for the delamination to advance one row of elements with ties at nodes across the delamination front being released according to their energy release rate exceeding G_C as shown in the plots of G_T for each frame. This process repeats one row at a time throughout propagation. This manner of delamination advancement through the mesh is not exactly physically accurate, as typically delaminations in a DCB specimen form a curved front that advances at the same rate across the width of the specimen, however, it is equivalent to the behavior seen in the high-fidelity benchmark model [23]. The large spikes in energy release rate located at corner nodes on the delamination front do not appear to cause any inaccuracies in the simulation of this specimen.

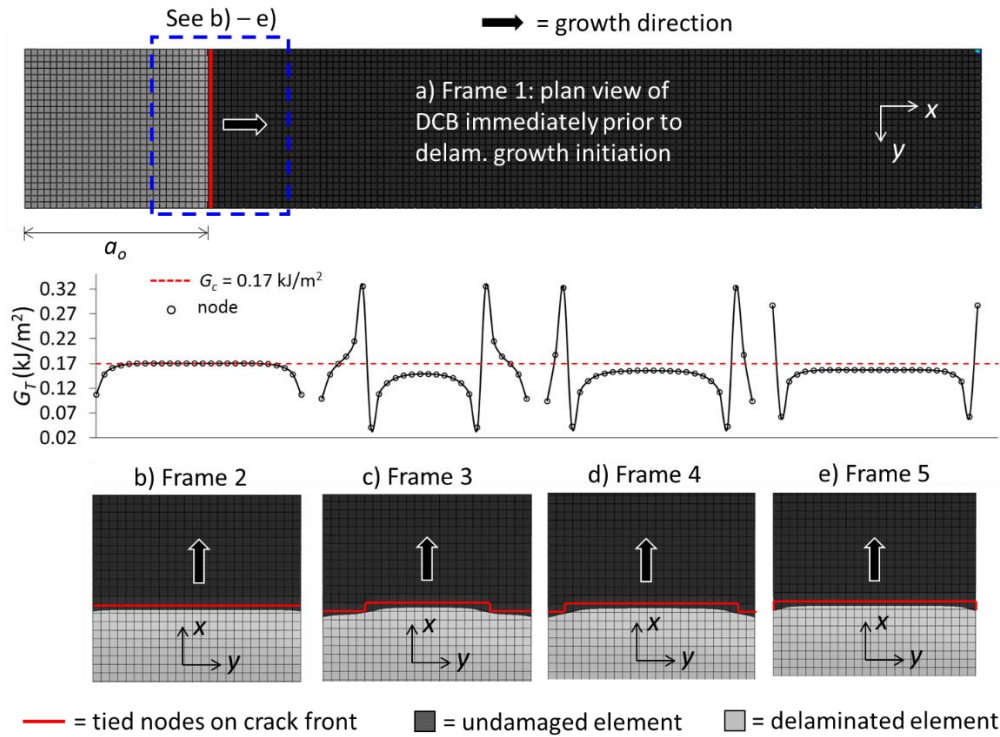


Figure 9. DCB: Delamination front geometry and energy release rate at the first instance of crack growth ($a = a_0 = 30.5$ mm).

CONCLUSIONS

A formulation was presented for a novel enriched shell finite element capable of delamination simulation in composite laminates. VCCT is combined with the Floating Node Method to simulate delamination growth at an arbitrary ply interface in a laminate layup. The element uses an adaptive splitting approach for damage characterization that allows for straightforward low-fidelity model creation and a numerically efficient solution.

The enriched shell element was verified for Mode I delamination simulation by comparing results against a numerical benchmark study. The mesh configuration in the vicinity of the delamination front was investigated and it was determined that ties connecting split elements should not constrain rotations and that more than one element ahead of the delamination must be split and tied together. Following these guidelines, the enriched element was shown to exhibit little mesh dependency while accurately predicting structural stiffness and energy release rate. More specifically, meshes sized to a crack extension length-to-laminate thickness ratio, $\Delta a/h$, of roughly 0.66 – 3.33 were all shown to result in accurate behavior. Investigation is ongoing in terms of mixed-mode delamination simulation and extension of the element enrichment to include transverse/out-of-plane type damage features such as matrix cracks.

REFERENCES

1. Heimbs, S., S. Heller, P. Middendorf, F. Hahnel, J. Weibe. 2009. "Low Velocity Impact on CFRP Plates with Compressive Preload: Test and Modelling," *International Journal of Impact Engineering* 36:1182-1193.
2. Davila, C.G., P. Camanho, A. Turon. 2008. "Effective Simulation of Delamination in Aeronautical Structures Using Shells and Cohesive Elements," *Journal of Aircraft*, 45(2):663-672.
3. Krueger, R. 2004. "Virtual Crack Closure Technique: History, Approach, and Applications," *Applied Mechanics Reviews* 57 (2):109-143.
4. Rybicki, E.F., M. Kanninen, 1977. "A Finite Element Calculation of Stress Intensity Factors by a Modified Crack Closure Integral," *Engineering Fracture Mechanics* 9 (4):931-938.
5. Wang, J.T., I.S. Raju, C.G. Davila, D.W. Sleight. 1993. "Computation of Strain Energy Release Rates for Skin-Stiffener Debonds Modeled with Plate Elements," *Proc. AIAA/ASME/ASCE/AHS 34th Structures, Structural Dynamics, and Materials Conference*.
6. Glaessgen, E.H., W.T. Riddell, I.S. Raju. 2002. "Nodal Constraint, Shear Deformation and Continuity Effects Related to the Modeling of Debonding of Laminates, Using Plate Elements," *Computer Modeling in Engineering & Sciences*, (3)1:103-116.
7. Krueger, R., K. Shivakumar, I.S. Raju. 2013. "Fracture Mechanics Analyses for Interface Crack Problems - A Review," *54th AIAA/ASME/ASCE/AHS/ASC Structures, Structural Dynamics, and Materials Conference, Boston, MA*.
8. Moes, N., J. Dolbow, T. Belytschko, 1999. "A Finite Element Method for Crack Growth Without Remeshing," *International Journal of Numerical Methods in Engineering* 46 (1):131-150.
9. Areias, P.M.A., J.H. Song, T. Belytschko. 2006. "Analysis of Fracture in Thin Shells by Overlapping Paired Elements," *Computer Methods in Applied Mechanics and Engineering* 195(41-43):5343-5360.
10. Chen, B.Y., S.T. Pinho, N.V. De Carvalho, P.M. Baiz, T.E. Tay, 2014. "A Floating Node Method for the Modelling of Discontinuities in Composites," *Engineering Fracture Mechanics* 127:104-134.
11. Larsson, R. 2004. "A Discontinuous Shell-interface Element for Delamination Analysis of Laminated Composite Structures," *Computer Methods in Applied Mechanics and Engineering* 193:3173-3194.
12. Nagashima, T., H. Suemasu. 2010. "X-FEM Analyses of a Thin-walled Composite Shell Structure with a Delamination," *Computers and Structures* 88:549-557.
13. Brouzoulis, J., M. Fagerstrom. 2015. "An Enriched Shell Element Formulation for Efficient Modeling of Multiple Delamination Propagation in Laminates," *Preprint submitted to Composite Structures*.
14. Dassault Systems. April 2, 2013. Abaqus[®] 6.14 Analysis User Manual.
15. Onate, E. 2013. Structural Analysis with the Finite Element Method. Linear Statics. Volume 2. Beams, Plates, and Shells. First Edition. International Center for Numerical Methods in Engineering, Barcelona, Spain.
16. Laitinen, M., H. Lahtinen, S.-G. Sjolind, 1995. "Transverse Shear Correction Factors for Laminates in Cylindrical Bending," *Communications in Numerical Methods in Engineering* 11:41-47.
17. De Carvalho, N.V., B.Y. Chen, S.T. Pinho, J.G. Ratcliffe, P.M. Baiz, T.E. Tay. 2015. "Modeling Delamination Migration in Cross-ply Tape Laminates," *Composites: Part A*, 71:192-203.
18. Orifici, A.C., R.S. Thomson, R. Degenhardt, S. Busing, J. Bayandor. 2007. "Development of a Finite Element Methodology for Modelling Mixed-mode Delamination Growth in Composite Structures," *12th Australian International Aerospace Congress, Australia*.
19. Xie, D., S.B. Biggers. 2006. "Strain Energy Release Rate Calculation for a Moving Delamination Front of Arbitrary Shape Based on the Virtual Crack Closure Technique. Part I: Formulation and Validation," *Engineering Fracture Mechanics* 73:771-785.
20. Ferrie, C.H., C.Q. Rousseau. 2001. "A Method of Applying VCCT to Corner Crack Nodes," *Proceedings of American Society for Composites, 16th Annual Technical Conference on Composite Materials, Blacksburg, VA*.
21. Benzeggagh, M.L., M. Kenane. 1996. "Measurement of Mixed-Mode Delamination Fracture Toughness of Unidirectional Glass/Epoxy Composites with Mixed-Mode Bending Apparatus," *Composites Science and Technology*, 56(4):439-449.
22. Cotterell, B., K. Hbaieb, J.G. Williams, H. Hadavinia, V. Tropsa. 2006. "The Root Rotation in Double Cantilever Beam and Peel Tests," *Mechanics of Materials* 38:571-584.

23. Krueger, R. 2014 "A Summary of Benchmark Examples and their Application to Assess the Performance of Quasi-static Delamination Propagation Prediction Capabilities in Finite Element Codes," *Journal of Composite Materials*, 0(0):1-20.
24. Sun, C.T., Jin, Z.-H. 2012. *Fracture Mechanics*. Elsevier, Inc.